1. Extended Data

-

Figure #	Figure title One sentence only	Filename This should be the name the file is saved as when it is uploaded to our system. Please include the file extension. i.e.: *Smith_ED_Fi_1.jpg*	Figure Legend If you are citing a reference for the first time in these legends, please include all new references in the Online Methods References section, and carry on the numbering from the main References section of the paper.
Extended Data Fig. 1	Comparing high- and low-resolution OVIRS spectra of Site #6	ExtendedData_abc-CS6.eps	a, The lower-resolution spectrum (magenta) of Site #6 shown in the main-text as compared to three higher-resolution pyroxene spectra obtained of Site #6 (teal) during a lower altitude (~1.5 km) regional flyby of Bennu by the OSIRIS-REx spacecraft. The lower-resolution spectrum (magenta) has been ratioed by Bennu's global average spectrum to bring out the subtle pyroxene absorption features near 1 and 2 µm, whereas the high-resolution spectra do not require any ratioing to observe these absorption features. b, The band I and II centers (1 and 2 µm) calculated for the pyroxene absorption features plotted against each other, for the lower-resolution (ratioed, magenta) and higher-resolution (unratioed, teal) spectra of Site #6. The spectral ratioing does not affect the band centers obtained beyond the uncertainty assigned by the fitting procedure. c, HCP% versus the ratio of the LCP to the HCP band strengths for the lower-resolution (ratioed, magenta) and higher-resolution (unratioed, teal) spectra of Site #6, which again shows that the ratioing procedure does not affect the results obtained by applying the MGM to these spectra.

Delete rows as needed to accommodate the number of figures (10 is the maximum allowed).

2. Supplementary Information:

A. Flat Files

Item	**Present?**	**Filename** **This should be the name the file is saved as when it is uploaded to our system, and should include the file extension. The extension must be .pdf**	**A brief, numerical description of file contents.** **i.e.: *Supplementary Figures 1-4, Supplementary Discussion, and Supplementary Tables 1-4.***
Supplementary Information	Yes	SupplementaryInformation_Pyroxene_on_Bennu_200714_FINAL.pdf	Supplementary Figures 1-9, Supplementary Tables 1-4
Reporting Summary	No		

Exogenic Basalt on Asteroid (101955) Bennu

D. N. DellaGiustina[1,2]*†, H. H. Kaplan[3]*†, A. A. Simon[4], W. F. Bottke[3], C. Avdellidou[5], M. Delbo[5], R.-L. Ballouz[1], D. R. Golish[1], K. J. Walsh[3], M. Popescu[6], H. Campins[7], M. A. Barucci[8], G. Poggiali[9], R. T. Daly[10], L. Le Corre[11], V. E. Hamilton[3], N. Porter[1], E. R. Jawin[12], T. J. McCoy[12], H.C. Connolly Jr.[13,1], J. L. Rizos Garcia[6], E. Tatsumi[6], J. de Leon[6], J. Licandro[6], S Fornasier[8], M. G. Daly[14], M. M. Al Asad[15], L. Philpott[15], J. Seabrook[14], O. S. Barnouin[10], B. E. Clark[16], M. C. Nolan[1], E. S. Howell[1], R. P. Binzel[17], B. Rizk[1], D. C. Reuter[4], and D. S. Lauretta[1]

(1) Lunar and Planetary Laboratory, University of Arizona, Tucson, AZ, USA. (2) Department of Geosciences, University of Arizona, Tucson, AZ, USA. (3) Southwest Research Institute, Boulder, CO, USA. (4) NASA Goddard Space Flight Center, Greenbelt, MD, USA. (5) Université Côte d'Azur, Observatoire de la Côte d'Azur, CNRS, Laboratoire Lagrange, Nice, France. (6) Instituto de Astrofísica de Canarias and Departamento de Astrofísica, Universidad de La Laguna, Tenerife, Spain. (7) Department of Physics, University of Central Florida, Orlando, FL, USA. (8) LESIA, Observatoire de Paris, Université PSL, CNRS, Université de Paris, Sorbonne Université, 5 place Jules Janssen, 92195 Meudon, France (9) INAF-Osservatorio Astrofisico di Arcetri, Florence, Italy (10) The Johns Hopkins University Applied Physics Laboratory, Laurel, MD, USA (11) Planetary Science Institute, Tucson, AZ, USA. (12) Smithsonian Institution National Museum of Natural History, Washington, DC, USA. (13) Department of Geology, Rowan University, Glassboro, NJ, USA. (14) The Centre for Research in Earth and Space Science, York University, Toronto, Ontario, Canada. (15) Department of Earth, Ocean and Atmospheric Sciences, University of British Columbia, Vancouver, British Columbia, Canada. (16) Department of Physics and Astronomy, Ithaca College, Ithaca, NY, USA. (17) Department of Earth, Atmospheric, and Planetary Sciences, Massachusetts Institute of Technology, Cambridge, MA, USA.

† These authors contributed equally to this work

***Corresponding authors:**
Daniella N. DellaGiustina (danidg@lpl.arizona.edu)
Hannah H. Kaplan (kaplan@boulder.swri.edu)

Summary Paragraph:

When rubble-pile asteroid 2008 TC$_3$ impacted Earth on October 7, 2008, the recovered rock fragments indicated that such asteroids can contain exogenic material [1,2]. However, spacecraft missions to date have only observed exogenous contamination on large, monolithic asteroids that are impervious to collisional disruption [3, 4]. Here we report the presence of meter-scale exogenic boulders on the surface of near-Earth asteroid (101955) Bennu—the 0.5-km, rubble-pile target of the OSIRIS-REx mission [5] which has been spectroscopically linked to the CM carbonaceous chondrite meteorites [6]. Hyperspectral data indicate that the exogenic boulders have the same distinctive pyroxene composition as the howardite–eucrite–diogenite (HED) meteorites that come from (4) Vesta, a 525-km-diameter asteroid that has undergone differentiation and extensive igneous processing [7, 8, 9]. Delivery scenarios include the infall of Vesta fragments directly onto Bennu or indirectly onto Bennu's parent body, where the latter's disruption created Bennu from a mixture of endogenous and exogenic debris. Our findings demonstrate that rubble-pile asteroids can preserve evidence of inter-asteroid mixing that took place at macroscopic scales well after planetesimal formation ended. Accordingly, the presence of HED-like material on the surface of Bennu provides previously unrecognized constraints on the collisional and dynamical evolution of the inner main belt.

We discovered six unusually bright boulders >1.5 m in diameter on the surface of Bennu (Fig. 1) in images acquired by the OSIRIS-REx Camera Suite (OCAMS) [10]. These boulders are observed in the equatorial to southern latitudes some are found in clusters, whereas others are more dispersed (Fig. 2a).

The bright boulders exhibit extremely different albedos than the bulk of the asteroid's surface, which has an average albedo of 4.4% [11, 12]. The global albedo distribution based on data from the OCAMS MapCam and PolyCam imagers is unimodal at centimeter scales [11]; however, these boulders are outliers at 13σ to 40σ above the mean (Fig. 2b; Supplementary Fig. 1). Furthermore, MapCam colour images show that the 0.70/0.85 µm band ratio of these boulders is distinct from that of the global average spectrum of Bennu (Fig. 2b). The band ratio suggests the presence of an absorption feature beyond 0.85 µm and is consistent with the presence of mafic minerals, such as pyroxene or olivine. The substantial albedo and colour deviation of this population of boulders, as well as their rarity, suggests a separate provenance from the rest of Bennu's regolith.

Spectra collected by the OSIRIS-REx Visible and InfraRed Spectrometer [13] show that these six bright boulders contain pyroxene, and not olivine, as indicated by a second absorption near 2 µm (Fig. 2c, Extended Data Fig. 1a). Pyroxene is a major rock-forming mineral in planetary materials, and numerous studies have quantitatively linked pyroxene compositions with spectral signatures in the visible and near infrared [14,15,16,17]. Pyroxenes can crystallize in different systems (monoclinic clinopyroxenes and orthorhombic orthopyroxenes) and with differing calcium cation chemistry. These factors influence the absorption bands I and II—near 1 and 2 µm—and yield a systematic relationship between high- and low-calcium pyroxene [14,15,18]. The bright boulders studied here have band I centers that range from ~0.90 to 0.95 µm and band II centers from ~1.95 to 2 µm (Fig. 3a, Extended Data Fig. 1b).

Although band centers can be used to distinguish between pyroxene compositions, they are less diagnostic for mineral mixtures that contain multiple pyroxenes. Thus, we also applied the Modified Gaussian Model [16] to OVIRS spectra of the bright boulders (Fig. 2c, Extended Data Fig. 1a); this allowed us to resolve overlapping absorption features near 1 and 2 µm that arise from different mafic silicates. A major application of MGM is to separate absorptions of high-calcium pyroxene (HCP) from those of low-calcium pyroxene (LCP) to estimate the abundance of HCP as a percentage of total pyroxene (HCP%). HCP% is an indicator of igneous differentiation in asteroids because as chondritic material melts, the partial melt is enriched in HCP, and the residue is strongly depleted in HCP [17].

We find HCP% values that range from 45 to 55%, indicating that the pyroxene identified on Bennu came from a body large enough to support igneous processes (Fig. 3b, Extended Data Fig. 1c). These values are not consistent with chondritic material, either from Bennu's parent body or from contamination by ordinary chondrites [17,19]. This composition, combined with the overall carbonaceous chondrite-like nature of Bennu, indicates that the observed pyroxene is exogenic. The alternative would require the formation of HCP as an incipient melt on Bennu's parent body, which is not compatible with the hydrated, phyllosilicate-rich composition of Bennu [6]. In terms of both estimated HCP% and band centers, the pyroxene-bearing boulders on Bennu correspond to HED meteorites, and in particular eucrites (Fig. 3a-b, Extended Data Fig. 1c-b).

A difference is that HED meteorites are nearly 5x brighter than the exogenic boulders that we observe on Bennu [20]. Laboratory studies, however, indicate that the reflectance of eucrite samples exponentially decreases as they are mixed with CM meteorite powders [21]; a similar effect can be observed by linearly combining spectra from carbonaceous chondrite and pyroxene from various meteorites in the visible wavelengths (Methods; Supplementary Fig. 3). On Vesta, dark terrains have been attributed to the infall of low-albedo carbonaceous material and have a reflectance that is 2-3x less than endogenous bright surface units [3, 4]. It is therefore possible that the exogenic boulders have been optically mixed with low-albedo endogenous material from Bennu, thereby decreasing their overall reflectance. Additionally, the pyroxene-bearing boulder with the highest albedo also shows the deepest 1-μm band (Fig. 2b), suggesting that boulder brightness may correspond to pyroxene exposure.

HED meteorites, as well as most pyroxene-rich basaltic objects in the inner main belt, are sourced from the vestoids [22, 23]—a family of asteroids that originated from, and have similar orbits to, Vesta [7, 8, 9, 22, 23]. This is likely the provenance of pyroxene-bearing boulders on Bennu, which have compositional homogeneity and are a close spectral match to the HED meteorites (Fig. 3a-b, Extended Data Fig. 1c-b). Furthermore, the population of inner main belt vestoids dynamically overlaps with the source regions of Bennu (Supplementary Fig. 8), providing a pathway for these boulders to be implanted on it or its parent body's surface [24, 25].

Dynamical models suggest that Bennu's parent body, which was >100 km, disrupted ~0.8 to 1.5 Ga ago from an inner main belt asteroid family, resulting in the formation of Bennu [24, 25]. After its formation, Bennu drifted across the inner main belt to a dynamical resonance that would take it to its current near-Earth orbit, a few Ma to tens of Ma ago [24, 25, 26]. En route, Bennu may have been impacted by one or more small vestoids, leaving behind the observed exogenic boulders. Alternatively, Bennu's parent body could have been contaminated by vestoids, which litter the present day inner main belt [8]. The impactors would have left behind meter-scale or larger material near or on the surface. When Bennu's parent body was subsequently disrupted, Bennu would have been created from a scramble of parent body and exogenic debris.

Laboratory collision experiments on porous surfaces show that up to 20% of a projectile's material can survive unmelted at low impact speeds < 2.6 km s^{-1} and vertical incidence [27, 28]. However, most impacts in the main belt would have occurred at higher velocities; we find that only 10 to 44% of all vestoids could have encountered Bennu at < 2.6 km s^{-1} (Methods). Although small projectiles moving at these low velocities could account for meter-sized exogenic boulders on Bennu, they cannot readily explain the multi-meter ones. This is because the progenitors of boulders ~4 m would require impactors so large that they should catastrophically disrupt Bennu, even at low impact velocities (Methods).

Another possibility is that Bennu accumulated from the remnants of a catastrophic collision between its precursor and a vestoid. Vestoids, however, do not dominate the present-day main belt at small sizes [29], and meteorites from Vesta only account for 6% of falls [30]. It is conceivable that circumstances existed shortly after the formation epochs of the vestoids, near 1 and 2 Ga ago [31, 32], where Vesta fragments dominated the main belt at small sizes for a brief period of time. Even so, the probabilities of creating and preserving Bennu under this scenario remain small (Methods).

This leads us to favor the parent body scramble scenario. Although modeling this scenario presents several complexities, the longer lifetime and larger surface area of the parent body relative to Bennu would have resulted in a higher number of probable impacts (Methods). Furthermore, the parent body was large enough to withstand high-velocity projectiles that would disrupt Bennu, increasing its overall number of probable impacts relative to Bennu. The parent body scramble scenario is also consistent with the geological setting of the exogenic boulders. Although half are proximal to putative impact craters, crater-scaling relationships show it is unlikely that the exogenic boulders produced those craters (Methods; Supplementary Fig. 5 and Tab. 2). Moreover, at Site 4, we observe bright pyroxene-bearing clasts embedded within the darker host matrix of a larger partially buried boulder (diameter ~ 5 m) whose overall colour and albedo are similar to Bennu's average surface (Fig. 1d, Supplementary Fig. 6). This suggests that the boulder is an impact breccia (rather than two distinct rocks), and comparable textures observed at Sites 2 and 3 may be further examples of breccias. If so, these would likely have originated on Bennu's parent body, because meter-scale brecciation requires energies that would disrupt Bennu [33, 34].

It is not yet clear why we observe HED-like boulders and no other exogenic material on Bennu, but higher-resolution data from regional OSIRIS-REx mission phases, and ultimately analysis of the returned sample, may reveal contributions from other impactors. For now, the presence of HED lithologies offers insights into other small asteroids; assuming that Bennu is representative, meter-scale exogenic material should exist on many and may not have been detected owing to observational limitations. This is consistent with prior studies which speculated that dark boulders found on the small (~0.3 km) S-type asteroid Itokawa are exogenous in origin [35]. Additionally, our observations complement the finding of ordinary chondrite–like boulders on (162173) Ryugu, the ~1-km rubble-pile target of the Hayabusa2 mission that is similar to Bennu in terms of its albedo and composition [36, 37, 38]. Differing exogenic lithologies on Bennu and Ryugu indicates they may have experienced different collisional histories.

The exogenic boulders on Bennu also provide context for recent discoveries of pyroxene clasts embedded in CM meteorites [39, 40]; conversely, xenolithic fragments of CM meteorites have been observed in some HEDs [41]. Our findings suggest that the OSIRIS-REx sample returned from Bennu may yield material that originated from Vesta. Such a finding could merge our understanding of the collisional processes observed on planetary surfaces with that of xenoliths observed in the meteorite collection.

Figure Captions

Figure 1 | In OCAMS PolyCam images, six unusually bright boulders exhibit a variety of textures. a, The boulder at Site 1 appears to have a flat, planar, exposed face (See Supplementary Fig. 9). b-c, Sites 2 and 3 are more angular and hummocky boulders with textures that indicate potential layering or brecciation. d, Whereas some bright boulders appear to be resting on the surface of the asteroid, Site 4 includes two bright pyroxene-bearing clasts that appear embedded within a large partially buried boulder whose albedo is similar to Bennu's average. As with Sites 2 and 3, this may be indicative of brecciation. e-f, The boulders at Sites 5 and 6 have variable albedos that change across their faces. The diffuse appearance may result from variable illumination caused by the texture of the boulder faces or be due to a layer of fine low-albedo dust coating the boulders. See Supplementary Table 1 for boulder dimensions.

Figure 2 | Physical and spectrophotometric properties of Bennu's bright pyroxene-bearing boulders. a, The bright pyroxene-bearing boulders (coloured circles) are observed in the equatorial to southern latitudes on Bennu and their distribution appears non-uniform, perhaps owing to resolution limitations at scales ≤1 m in global OSIRIS-REx MapCam data. The diameter of each circle indicates the relative size of the boulder (not to scale with the background basemap). Three boulders form a cluster near 60° longitude, but the others are more distributed. **b**, The 0.70/0.85 μm band ratio for each boulder from MapCam (~25 cm/pixel) versus its panchromatic normal reflectance from PolyCam data (~7 cm/pixel). Colors correspond to panel a and error bars signify the radiometric uncertainty of reflectance values (Methods). Bennu's global average 0.70/0.85 μm band ratio and normal reflectance are shown for context (dashed lines) along with their 1σ variation (blue shaded envelopes). **c**, The OVIRS spectrum for each site (colors correspond to panel a) divided by the global average OVIRS spectrum of Bennu. The OVIRS spot size is ~20 m for these spectra; therefore, the boulders occupy <1% of the field of view (Supplementary Fig. 2). Dividing by the global average spectrum of Bennu highlights the subtle absorption features associated with the boulders. The band depth at 0.92 μm (dashed line) is labeled for each spectrum just below the absorption feature to show the relative strength of the band I center for every boulder.

Figure 3 | Bennu's bright pyroxene-bearing boulders are spectrally similar to the HED meteorites. a, The band centers for the 1- and 2-μm absorption features plotted against each other for spectra of bright pyroxene-bearing boulders on Bennu. Band centers for several HED meteorites [18] and synthetic pyroxene samples are shown for context [15]. Error bars signify the standard deviation from the Monte Carlo fitting procedure used to estimate the band centers (see Methods). Site 5 was excluded from this analysis as its spectrum possessed a low signal-to-noise ratio. b, HCP% versus the ratio of the LCP to the HCP band strengths for bright pyroxene-bearing boulders on Bennu, as determined by applying the MGM to OVIRS spectra. The ranges for meteorites, including eucrites, ordinary chondrites, and lodranites, are shown for context [17]. Error bars signify the standard deviation from the Monte Carlo fitting by the MGM (see Methods). Sites 4 and 5 were excluded from this analysis as their OVIRS spectra possessed low signal-to-noise ratios that interfered with fitting by the MGM.

Methods

Image data processing

Bennu's average terrain exhibits a much lower albedo than the exogenic boulders described in this study. Thus, in many MapCam and PolyCam images, these boulders are saturated. All reflectance information reported here is obtained from unsaturated pixels (>98% radiometric linearity); saturated pixels (DN > 14000 in uncalibrated Lo MapCam images, DN > 12500 in uncalibrated Lo PolyCam images; [42]) were discarded from our analysis. OCAMS images are calibrated into units of reflectance (also known as radiance factor or *I/F*) with a 5% absolute radiometric uncertainty according to procedures described by Golish et al., (2019) [42]. Images were photometrically corrected to I/F values at 0° phase angle, 0° emission angle, and 0° incidence angle (0°, 0°, 0°) and (30°, 0°, 30°) using the ROLO phase function and Lommel-Seeliger disk function as described by Golish et al., 2020 [43].

MapCam colour images that first detected the pyroxene-bearing boulders were acquired on March 14, 2019, from 17:37 to 22:19 UTC, and their presence was confirmed in colour images acquired on September 26, 2019 from 17:12 to 21:50. Both days of MapCam observations provided global coverage with an approximate pixel scale of ~25 cm, phase angle of ~8.5° and local solar time (LST) of ~12:49PM. For each boulder, the data were acquired in nearly identical colour sets taken at short, medium, and long exposure times; we selected short-exposure sets for our analysis to avoid saturated pixels. Even for the lowest exposure times, however, 50% of the pixels were removed due to saturation at Site 1 for the data obtained March 14, 2019. Hence, we used the low-exposure-time data from September 26, 2019, for determining band ratios, as those data did not experience saturation. The global MapCam panchromatic normal reflectance map was used to determine the global reflectance distribution of Bennu at a pixel scale of ~32 cm. It is constructed from 12:30PM LST images collected from 17:39 to 22:21 UTC at a phase angle of ~8°. To the measure colour and reflectance information, MapCam images were registered to the tessellated global shape model of Bennu (v28; 80-cm ground sample distance (GSD)) [44] using the Integrated Software for Imagers and Spectrometers version 3 (ISIS3). Mosaics and colour cubes were produced using techniques described by DellaGiustina et al., 2018 [45].

PolyCam panchromatic images used to determine boulder panchromatic normal reflectance include: 20190307T173147S243_pol_iofL2pan.fits (Site 1), 20190328T194159S619_pol_iofL2pan.fits (Site 2 and 3), 20190321T191242S629_pol_iofL2pan.fits (Site 4), 20190321T190056S516_pol_iofL2pan.fits (Site 5), and 20190321T184411S010_pol_iofL2pan.fits (Site 6). For Sites 2 to 6, the images used to calculate the normal reflectance of exogenic boulders were chosen based on the highest available resolution (~5.25 cm/pixel) and lowest available emission angle. For Site 1, we selected an image with a pixel scale of ~7 cm and the lowest available exposure time and no saturated pixels, as this boulder is overexposed in higher resolution images. At short exposure times, however, PolyCam data experience a high degree of charge smear and 'icicle' artifacts [42]. The OCAMS PolyCam charge smear correction algorithm depends on the image data to determine the amount of signal to remove and is less accurate for images with icicles, as these artifacts overwrite the valid data that inform the correction algorithm. This yields a lower-fidelity charge smear correction and results in an additional uncertainty of 5% in short-exposure-time data. To measure the dimensions and panchromatic reflectance of the exogenic boulders, PolyCam images were registered to high-resolution digital terrain models (5 to 6 cm GSD) produced from OSIRIS-REx Laser Altimeter (OLA) data [46].

Using ISIS3, reflectance values in PolyCam and the four MapCam bands were obtained by manually tracing polygons around each pyroxene-bearing boulder in the panchromatic and colour image cubes, and extracting the average pixel value from within the polygons.

PolyCam images that characterize the overall size and morphology of pyroxene boulders were acquired on several days under varying illumination conditions throughout the Orbital A and Detailed Survey mission phases [5] and include: 20190321T201326S593_pol_iofL2pan.fits, 20190328T194159S619_pol_iofL2pan.fits, 20190321T190958S257_pol_iofL2pan.fits, 20190307T-203057S263_pol_iofL2pan.fits 20190307T203526S248_pol_iofL2pan.fits, and 20190227T041127S994_pol_iofL2pan.fits.

Spectral data processing

Global OVIRS data used in this study were obtained from a 5-km altitude flyby which resulted in a ~20 m instrument spot size (not accounting for along-track smear; see Supplementary Fig. 2). Thus, in global observations, the pyroxene boulders described here occupy <1% of the field of view of OVIRS spectra. For completeness, we also examined data collected by the OSIRIS-REx Thermal Emission Spectrometer [OTES; 47] over the same areas, but no distinct signatures for pyroxene have been confidently detected in them. This is likely because OTES data cover sufficiently large areas (~40 m instrument spot size, not accounting for along-track smear) such that the pyroxene boulders are a minute fraction of the field of view.

Global OVIRS data were acquired at 12:30PM and 10:00AM LST during the Detailed Survey Equatorial Station observations on May 9, 2019 and May 16, 2019, respectively. Spectra were obtained in north-to-south spacecraft scans that mapped Bennu's surface as the asteroid rotated. Individual filter segments are converted from calibrated radiance to I/F by resampling onto a continuous wavelength axis, subtracting a modeled thermal emission, and dividing by range-corrected solar flux [48]. In these global data, the spectral signatures associated with pyroxene have very shallow band depths of 1% or less, and the best method for displaying them is to divide by a global average spectrum to remove any spectral artifacts or other globally prevalent absorption signatures. The global average was calculated using ~2000 OVIRS spectra acquired at the same LST and has a weak linear blue slope of less than -1% per 100 nm from 0.5-2.5 µm (Supplementary Fig. 4). After dividing all spectra by the global average, regions with potential pyroxene signatures were identified by a manual search and by an automated search for a broad absorption feature at 0.92 µm. Both methods identified the same locations for the strongest signatures, corresponding to the brightest boulders in OCAMS images.

Ratioing these spectra by the global average removed artificial discontinuities that correspond to the OVIRS filter segment boundaries at 0.65, 1.05 and 1.7 µm, and also eliminated the presence of ubiquitous narrow absorption features at 1.4, 1.9 and 2.3 µm that are not associated with pyroxene. Additionally, we obtained an opportunistic regional OVIRS observation of the Site #6 pyroxene at higher-resolution (~5 m spot size) during a low-altitude (~1.4 km) flyby performed on October 26, 2019 at 20:07 UTC (Extended Data Fig. 1a). During this observation, the Site #6 boulder more completely filled the OVIRS field of view; thus, the pyroxene absorption features are clearly present, and there was no need to ratio these spectra with the global average spectrum of Bennu. Comparing higher-resolution spectra of Site #6 (unratioed) to those obtained at lower resolution (ratioed) indicates that the ratioing procedure used here does not influence the results of our analyses beyond the assigned uncertainties (Extended Data Fig. 1).

In the global data, the OVIRS field-of-view was continuously scanned across the surface and regions with sharply contrasting features can show "jumps" in the spectrum from 0.4 to 0.66 µm or 0.66 to 1.08 µm, as different wavelength regions were acquired over a slightly different part of the surface. Thus, the manual inspection was necessary to rule out false positive pyroxene detections and to identify other nearby spectra that were missed in the automated search. Any "jumps" were corrected by adjusting that portion of the spectrum to match the absolute brightness of the spectrum on either side of the jump. Co-located detections were averaged together to produce a site-averaged spectrum, which was then smoothed using a 3-sigma Gaussian kernel. Finally, the continuum was removed using a linear fit between 0.7 and 2.5 µm. Uncertainties in 0.92-µm band depth were estimated using a five-channel standard deviation in the unsmoothed data.

To determine band centers, we fit Gaussian curves to the 1- and 2-µm pyroxene absorptions in the continuum-removed ratioed spectra and found the Gaussian center wavelength. We used a Monte Carlo approach, in which the initial Gaussian centers were varied by a random value less than or equal to ± 0.05 µm and the best fit was recorded for each of 10,000 model fits to determine the uncertainty on our estimated band centers. A similar approach was used to resolve individual absorptions.

To resolve pyroxene absorptions due to HCP and LCP, we applied the MGM to OVIRS data from 0.4 to 2.6 µm and fit six to seven Gaussians to the region after analyzing initial runs [49]. Of these Gaussians, two were fit to LCP absorptions (~0.92 and 1.90 µm) and three to HCP absorptions (1.00, 1.20, and 2.30 µm) [17]. In the model, Gaussian curves are superimposed on a baseline continuum, which is linear in wavenumber space, and the model is inverted to solve for Gaussian center, amplitude, and width, and the continuum simultaneously. Model constraints control the magnitude of change possible for each of these parameters and do not allow for unphysical solutions (e.g., inverted Gaussians). Supplementary Table 3 and 4 provide the MGM fit and Gaussians used in this analysis.

We used a Monte Carlo approach to calculate uncertainty on model output parameters by systematically varying the model starting conditions. Although the MGM has built-in methods for estimating uncertainty on each model parameter from known physical properties, we have limited knowledge of a priori uncertainty given that these are spacecraft detection of unknown materials with unknown origin. Therefore, we ran the model 10,000 times and changed the initial Gaussian band center estimates for each of the seven Gaussians by an independent, random number normally distributed between ± 0.50 µm (or approximately 10 OVIRS channels) for each model run. We recorded initial band positions and model results, using the full set of 10,000 runs to estimate uncertainty values on each parameter; a model was considered successfully fit if the full set of results converged and we found that in all cases, we were able to use the same set of starting parameters and achieve model convergence.

Average Gaussian amplitudes from the MGM runs were used to calculate the "component band strength ratio" [49], or the ratio of LCP to HCP band strengths. We use the ratio of band strengths in the 1-µm band, rather than the 2-µm band, because of potential uncertainty in 2-µm band calibrations due to temperature [18].

Spectral mixing model

We constructed a simple linear mixing model to assess whether the lower albedo of pyroxene-bearing boulders on Bennu, relative to that of HED meteorites, can be explained by combining the spectra of CI/CM chondrites and achondritic pyroxenes. Specifically, we used a "checkerboard" approach [50] that assumes that the compositions are optically separated, so that multiple scattering occurring between the constituents is negligible.

We considered an areal ratio in the order of A% for the basaltic material and B% for carbonaceous material. The combination can be expressed with the formula $R_f = A \times R_{PYX} + B \times R_{CC}$, where R_f is the reflectance spectrum, R_{PYX} is the median spectrum of meteoritic pyroxenes, and R_{CC} is the median spectrum of CI/CM chondrites. We applied the model to linear combinations of achondritic and CM/CI meteorite spectra from RELAB [51]. By searching all possible combinations, we found that the spectrophotometric match observed for the MapCam pyroxene-bearing boulders is best fit by linear combinations of 5–20% of various meteoritic pyroxenes with 95–80% carbonaceous chondrites (CMs and CIs). This is exemplified in Supplementary Fig. 3, which shows that a small amount of basaltic material mixed with CM material can result in the observed effect. The best fit obtained for the pyroxene-bearing boulder in Site 1 corresponds to a combination of the spectrum (A = 20%) of ALHA77005,193 pyroxene (Sample ID: DD-MDD-034, RELAB file: C1DD34) with the spectrum (B = 80%) of the Murchison meteorite (Sample ID: MS-CMP-002-E, RELAB file: CEMS02).

Collisional model

We examined whether Bennu or its parent body could have been plausibly contaminated by debris from the vestoids. We also explored whether the pyroxene-bearing boulders could have come from the disruption of Bennu's contaminated parent body. For the latter, we assume that Bennu is a first-generation rubble pile based on work which shows that the fraction of bodies that escape the Polana and Eulalia asteroid families are dominated by first-generation objects [52]. This is in contrast to the possible intermediate parent-body stages for the asteroid Ryugu [37], inferred in part by its partial dehydration, which is not observed on Bennu [6]. Our work takes advantage of established methods and codes (e.g., Bottke et al. 1994 [53]; Avdellidou et al. 2018 [54]; Briani et al. 2011[55]; Gayon-Markt et al. 2012 [56]; Turrini et al., 2014 and 2016 [57, 58]).

For the population of projectiles, we considered the present-day Vesta family, which includes 15,238 known asteroids with proper semi-major axis between 2.24 and 2.48 AU, 0.075–0.133 proper eccentricity, 5–8° proper inclination, and absolute magnitude H between 12 and 18.3 [59]. Diameters (D) have been measured for 1889 of these asteroids; when the diameter is not known, it is possible to estimate it using the average geometric visible albedo $p_V = 0.34$ of the family and the H values of each asteroid with the equation $D(\text{km}) = 1329\,(p_V)^{-1/2}\,10^{(-H/5)}$. The cumulative size-frequency distribution for asteroids with $12 < H < 17$ (the upper limit corresponds to the current completeness of the main belt) can be fit by a power law of the form $N_{vestoids} = D^a 10^b$ with $a = -2.5$ and $b = 4.1$, allowing us to extrapolate the Vesta family population to sizes smaller than what is currently observable (Supplementary Fig. 7). Because we expect that the Vesta family has lost members by collisional grinding, the present-day vestoid population represents a lower limit. In particular, the vestoids likely formed at two different epochs, near 2 and 1 Ga ago, linked to the formation of the Veneneia and Rheasilvia basins on Vesta [31, 32]. As a result, the first generation of vestoids experienced a decline at D >1 km due to collisional grinding, before being combined with the second generation.

First, we assessed the possibility of vestoid contamination of Bennu's parent body. Using the present-day Vesta family, we calculated the intrinsic collision probability, P, and the impact velocity, V, between a representative set of vestoids and Bennu's parent body given their semimajor axes (a), eccentricity (e), and inclination (i) (e.g., see [53] for methodology). Dynamical models indicate that the source region of Bennu could be the Polana (sometimes referred to as New Polana) or Eulalia asteroid families [24], with a 70% and 30% probability, respectively [24]. Accordingly, we considered each family's largest remnant as the putative parent bodies: (142) Polana, with proper (a, e, i) of (2.4184 au, 0.1576, 3.316°), and (495) Eulalia, with proper (a, e, i) of (2.4868 au, 0.1185, 2.516°). The sizes of the Eulalia and Polana parent bodies were estimated to be at least 100 to 200 km in diameter, respectively [24]. We found that the average impact probability $\langle P \rangle$ of vestoids impacting Polana and Eulalia is 8.9×10^{-18} and 8.6×10^{-18} impacts km^{-2} yr^{-1}, respectively, with corresponding average impact velocities $\langle V \rangle$ of 3.5 and 4 km s^{-1}.

Next we considered direct contamination of Bennu's surface from meter-scale vestoid fragments. We modeled Bennu test asteroids (assuming a 250 m radius) that were located within the Polana and the Eulalia families at six different plausible locations in (a, e, $\sin i$) space (Supplementary Fig. 8). For the six test asteroids, the value of $\langle P \rangle$ varies between 8.8×10^{-18} and 1.3×10^{-17} impacts km^{-2} yr^{-1}, and average impact velocities $\langle V \rangle$ between 3.3 and 4.2 km s^{-1}. We modified our algorithm to account for orbital intersections that correspond to lower impact velocities, $V < 2.6$ km s^{-1}, for which we expect at least 20% of projectile material to be retained as unmelted fragments on the porous granular target after impact [27, 28]. We note here that observations of brecciated lithologies that included unmelted fragments were reported by Daly and Schultz [60, 61] indicating that it is plausible for such fragments to be implanted at velocities up to 5 km s^{-1}, though the proportion of unmelted material was not directly quantified by their studies. Due to the different techniques to quantify the retention of preserved impactor material, we prefer to remain conservative and use as cutoff $V < 2.6$ km s^{-1}, noting that a higher cutoff velocity will improve the likelihood of the scenarios under consideration here. Using the cutoff of $V < 2.6$ km s^{-1} also minimizes the possibility that Bennu would have been catastrophically disrupted by the projectiles considered (see Crater Scaling Model methods).

For the scenario where the impact velocity is $V < 2.6$ km s^{-1} we find that $<P>$ of vestoids impacting Polana and Eulalia is 1.4×10^{-18} and 2×10^{-18} impacts km^{-2} yr^{-1}, respectively. On the Bennu test asteroids, $<P>$ ranges 1.4×10^{-18} to 3.9×10^{-18} impacts km^{-2} yr^{-1}. This demonstrates that average impact probabilities $<P>$ of Vesta family members impacting Polana, Eulalia, and Bennu (while it was in the main belt) are of the same order of magnitude. From the ratio of probabilities calculated above with constrained and unconstrained impact velocities, we conclude that between 16% (for Polana) and 23% (for Eulalia) of vestoids were available to impact Bennu's parent body at $V < 2.6$ km s^{-1}. Depending on whether its prior location was within either the Polana and Eulalia families, as modeled by our six test asteroids, we find that anywhere from 10 to 44% of vestoids were available to impact Bennu directly at $V < 2.6$ km s^{-1}. This demonstrates that based on impact probability alone, the likelihood of low-speed impacts between Bennu or its parent body and Vesta's fragments are non-negligible. However, Eulalia and Polana would still capture more impactors by virtue of their larger cross-sectional areas (exceeding Bennu's by a factor of 10^4 to 10^5).

We further assessed the likelihood of whether or not slow-moving impactors from the Vesta family could have been added to Bennu. The number of impacts, N, that a target can undergo from a specific projectile population can be approximated by [62]: $N = <P> (A/\pi)\, \Delta T\, N_{proj}$, where A is the sum of the cross-section of the target and of each impactor (i.e., π is included in $<P>$, so we scale the A value by π), ΔT is the time interval and N_{proj} is the number of potential impactors in a diameter range D (e.g. $N_{proj} = dN/dD\, \Delta D$). We assumed that ΔT was 1 Ga, the approximate age of Bennu's source family [24], and that $(A/\pi) = 0.0625$ km^2 (using a 250 m radius for Bennu). Poisson statistics control the number of impacts on a target; therefore, we set $N = 3$ to have reasonable (95%) probability of at least one impact. By calculating $<P>$ values for six Bennu test asteroids, we determined that N_{proj} needs to be between 1.2×10^{10} and 3.4×10^{10} in order for Bennu to have a 95% chance of experiencing at least one impact from a vestoid. We find that such values of N_{proj} in the Vesta family size distribution correspond to meter-scale vestoids. Accordingly, it is plausible that some meter-scale objects were added to Bennu.

While it is possible for meter-sized objects to strike Bennu at low velocities, we have not yet accounted for how the projectiles will fragment upon impact. Our expectation is the surviving boulders will be smaller than the observed boulders. It is possible that by adjusting parameters (e.g. considering impact speeds than <4 km s^{-1}), we could deliver meter-scale boulders, for example 4 m in diameter, but that would not explain the existence of the observed and intact 4 m boulder on Bennu.

An alternative scenario is that Bennu's parent body was contaminated by sufficient pyroxene impactors that its disruption could plausibly produce the observed vestoid-like boulders on Bennu. Our goal here is to conduct a plausibility study, such that certain details of the problem will be ignored for now. We believe there are certain advantages in this hypothesis: (i) Bennu's parent body is large enough to withstand the impacts of Vestoids that are many kilometers in size without difficulty, (ii) fragments produced by such an impact can easily be both 1 to 4 m meters in size, and (iii) laboratory shot experiments into porous materials indicate that craters on large carbonaceous chondrite bodies form in the compaction regime and produce little ejecta; this suggests that considerable mass from the projectile would remain bound to the parent body

[63, 64].

For constraints, we first examined the meter-scale pyroxene-bearing boulders on Bennu. Their net volume is at most ~70 m^3 (Supplementary Table 1). We assumed that these boulders contaminated an exterior shell on Bennu that is 3 to 5 m deep, yielding a volume of 2.3×10^6 m^3 to 3.9×10^6 m^3. If we assume that Bennu's interior is as contaminated by exogenic boulders as its surface, the ratio of the two values, 3×10^{-5} to 1.8×10^{-5}, tells us the fraction of vestoid material that had to be included into the parent body material that ultimately made Bennu. We call this target contamination value C_{target}.

Using the diameters above, the estimated volumes of Eulalia and Polana are 5.2×10^{14} m^3 to 4.2×10^{15} m^3. As an upper limit, we assumed that any basaltic material that struck the surface of these bodies remained [63, 64]. If Bennu came from a disruption event that completely mixed the contaminated surface of the parent body with its interior, the net volume of vestoids able to reproduce C_{target} corresponds to spherical impactors with diameters of 2.6 to 3.1 km and 5.3 to 6.2 km for the 100- and 200-km parent bodies, respectively. The question is whether this is plausible given what we know about the existing population of the Vesta family.

Using the equation $N = \langle P \rangle \, (A/\pi) \, \Delta T \, N_{\mathrm{proj}}$, we can determine whether any of these projectile sizes could have plausibly hit Bennu's parent body prior to its disruption. Using the data from the present-day Vesta family (as shown in Supplementary Fig. 7), we find that $N_{\mathrm{proj}} = 446$ and 30 for objects that range in diameter from 2.6 to 3.1 km and 5.3 to 6.2 km, respectively. The cross-section of the parent body is in the range of A/π = 2500 km^2 (for a 100-km diameter) to 10000 km^2 (for a 200-km diameter). As derived above, $\langle P \rangle$ is 8.9×10^{-18} km^{-2} yr^{-1} to is 8.6×10^{-18} km^{-2} yr^{-1} for Polana and Eulalia, respectively. If N = 3, we find that time ΔT needed to get the C_{target} level of contamination for the 100-km Eulalia parent body is 31 Ga, while for the 200-km Polana parent body, it is 112 Ga. These values are much longer than the age of the Solar System, so we can reject this scenario as described.

A more plausible scenario may be that the exterior shell of Bennu's parent body was contaminated by multiple vestoids, and these were among the debris that reaccumulated to form Bennu following catastrophic disruption. Such a scenario would require us to consider many additional aspects of the collisional evolution of the vestoids (e.g., [65]). For example, the Vesta family size frequency distribution shown in Supplementary Fig. 7 represents a simple estimate of the initial family size distribution, but collisional evolution over the age of the family (as linked to the formation of the Rheasilvia and Veneneia craters on Vesta) would require additional changes to reproduce the present-day family (e.g., additional $D >$ 1-km bodies). This could lead to enhanced contamination, which in turn could compensate for the possibility that the fraction of projectile material retained on the parent body is less than 1 (e.g., [57]; [63]). Another factor is that Bennu's parent body could have sustained impacts from vestoids linked to the formation Veneneia basin, ~2 Ga ago [31, 32] and prior to Bennu's formation ~ 1 Ga [24, 25, 26]. This would increase the likelihood that the contamination occurred on the parent body rather than on Bennu.

Modelling these scenarios is complicated for several reasons: (1) There are no observational constraints on the sub-kilometer population of vestoids. Thus, at a minimum, the extrapolated size-frequency distribution cannot exceed the estimated ejected volumes of the basins on Vesta. (2) Collisions with main belt bodies disrupt the Vesta family over time, and larger disruption events partially replenish the population of small vestoids. The observed vestoid population loses bodies, so it represents a lower limit, while the estimated extrapolated population does not account for collisional grinding, so it represents an upper limit. (3) It is necessary to consider the formation ages of the Rheasilvia and Veneneia basins, whose creation produced different components of the Vesta family, and the disruption age of Bennu's parent body, which was struck by vestoids. In particular, because Rheasilvia basin overprints Veneneia, the surfaces of Veneneia were likely modified by the later event. Accordingly, although Veneneia's estimated crater retention age is ~2 Ga, the real age of Veneneia, as well as the oldest portion of the Vesta family, may be much older. Knowledge of the precise age of Veneneia could help test our hypothesis.

Overall, however, computations performed here illustrate that it is plausible that vestoids could have been added to either Bennu or its parent body. However, Bennu can likely only withstand impacts of lower speed, whereas the parent body could capture more impactors due to its larger cross-sectional area and ability to withstand higher-velocity collisions. Thus, it is more likely that contamination occurred on the parent body than on Bennu.

Crater Scaling Model

We identified craters spatially associated with five of the six exogenic boulder sites. Sites 1, 2, and 3 are clustered in and around a 42 m-diameter crater, Site 4 is close to the center of an 83 m-diameter crater, and Site 6 is located in the southern wall of a 128-m-diameter crater. Although crater co-location may suggest a common origin, indicating direct delivery to Bennu, crater scaling and catastrophic disruption laws suggest otherwise.

There are two scenarios that may explain exogenic boulders in the context of direct contamination of Bennu: 1) three individual impacts that created the associated craters and left behind proximal pyroxene-bearing boulders, or 2) a single impact event that produced a single crater, resulting in proximal and distal pyroxene-bearing boulders. For both scenarios, we considered hypervelocity impacts at speeds of 3 km s^{-1} and 5 km s^{-1} with corresponding projectile retention efficiencies of 20% [28] and 7% [66].

For the first scenario, the projectile retention efficiencies were used to derive the original diameter of the pyroxene-bearing projectile corresponding to each of the three craters (labeled filled circles in Supplementary Fig. 5). We combined the volumes of the pyroxene-bearing boulders in Sites 1, 2, and 3 to calculate the size of a single projectile that created the co-located 42-m-diameter crater. We compared the relationship between the projectile and crater sizes to strength- and gravity-dominated crater scaling laws [66]. For both the 3 km s^{-1} and 5 km s^{-1} cases, the measured crater diameter is inversely proportional to the calculated projectile size (Supplementary Table 2). This is contrary to crater scaling expectations, suggesting that a multiple-impact scenario directly on Bennu is an unlikely explanation for the origin of the exogenic boulders.

For the second scenario, the volumes of all six boulders were combined. The diameter of a single pyroxene-bearing progenitor was then calculated for each impact speed case using the corresponding projectile retention efficiency (unlabeled open circle in Supplementary Fig. 5). We used the largest co-located crater (128-m diameter) to compare with crater scaling laws. We obtained an upper limit for a projectile size by using the catastrophic disruption threshold for impacts onto a porous target [63, 64] with Bennu's size and bulk density [44] (shaded region in Supplementary Fig. 5).

We find that an impact at 5 km s^{-1} by a single progenitor would exceed the catastrophic disruption threshold (Supplementary Fig. 5b). An impact by that same progenitor at 3 km s^{-1} is below the threshold (Supplementary Fig. 5a), and lies along the strength-dominated crater scaling relation (Supplementary Fig. 5a). This crater-scaling relation indicates a crater retention surface age of 0.1-1.0 Ga for the surface of Bennu [33], which is compatible with the direct contamination collisional model outlined in the previous section. However, we note the presence of a crater on the surface of Bennu with a diameter in excess of 200 m that, if similarly scaled, would suggest an associated impactor with a specific impact energy that would exceed the catastrophic disruption threshold.

Based on measurements of the craters on Bennu [33] and crater scaling laws, we find that direct contamination on to Bennu by pyroxene projectiles is difficult. Of the scenarios explored here, the only feasible pathway for direct contamination on Bennu would be an impact by a single 10.5-m-diameter pyroxene projectile at a speed of 3 km s^{-1}. However, this would suggest a strength-dominated crater scaling relationship (as shown by the open circle in Supplementary Fig. 5a, which lies on the solid red line). Use of a strength-dominated scaling relationship implies that Bennu should have already been catastrophically disrupted by the impactor that formed its largest craters (as the corresponding impactor diameter for such a crater lies right on the catastrophic disruption threshold). Thus, it seems unlikely that a strength-dominated scaling law is completely appropriate for Bennu, and therefore a direct contamination scenario less plausible.

Data availability: The OCAMS (MapCam and PolyCam), OLA, and OVIRS data that support the findings and plots within this paper are available from the Planetary Data System (PDS) at https://sbn.psi.edu/pds/resource/orex/ocams.html, https://sbn.psi.edu/pds/resource/orex/ola.html, and https://sbn.psi.edu/pds/resource/orex/ovirs.html, respectively. Data are delivered to the PDS according to the schedule in the OSIRIS-REx Data Management Plan, available in the OSIRIS-REx mission bundle at https://sbnarchive.psi.edu/pds4/orex/orex.mission/document/. Data shown in Supplementary Figs. 7 and 8 were obtained from the Minor Planet Physical Properties Catalogue (MP3C, https://mp3c.oca.eu/) of the Observatoire de la Côte d'Azur.

Code availability: The collisional analysis reported here uses a custom code that is based established methods described in Bottke et al. 1994 [53]; Avdellidou et al. 2018 [54]; Briani et al. 2011[55]; Gayon-Markt et al. 2012 [56]; Turrini et al., 2014 and 2016 [57, 58]). The ISIS3 code used to generate the image processing data products is a customized version of code available from the US Geological Survey–Astrogeology Science Center: https://isis.astrogeology.usgs.gov/. The MGM code used to analyze OVIRS spectral data is available from RELAB at Brown University: http://www.planetary.brown.edu/mgm/

Letter References:

1. Jenniskens, P. A. et al. The impact and recovery of asteroid 2008 TC3. Nature 458, 485 (2009).
2. Bischoff, A., Horstmann, M., Pack, A., Laubenstein, M. & Haberer, S. Asteroid 2008 TC3—Almahata Sitta: A spectacular breccia containing many different ureilitic and chondritic lithologies. *Meteoritics & Planetary Science* **45**, 1638-1656 (2010).
3. McCord, T. B. et al. Dark material on Vesta from the infall of carbonaceous volatile-rich material. *Nature* **491**, 83-86 (2012).
4. Reddy, V. et al. Delivery of dark material to Vesta via carbonaceous chondritic impacts. *Icarus* **221**, 554-559 (2012).
5. Lauretta, D. S. et al. OSIRIS-REx: sample return from asteroid (101955) Bennu. *Space Science Reviews* **212**, 925-984 (2017).
6. Hamilton, V. E. et al. Evidence for widespread hydrated minerals on asteroid (101955) Bennu. *Nature Astronomy* **3**, 332-340 (2019).
7. Consolmagno, G. J. and Drake, M. J. Composition and evolution of the eucrite parent body: Evidence from rare earth elements. *Geochim. Cosmochim. Acta* **41**, 1271-1282 (1977).
8. Binzel, R. P., and Xu, S. Chips off of Asteroid 4 Vesta: Evidence for the Parent Body of Basaltic Achondrite Meteorites. *Science* **260**, 186-191 (1993).
9. Russell, C. T. et al. Dawn at Vesta: Testing the protoplanetary paradigm. *Science* **336**, 684-686 (2012).
10. Rizk, B. et al. OCAMS: the OSIRIS-REx camera suite. *Space Science Reviews* **214**, 26 (2018).
11. Lauretta, D. S. et al. The unexpected surface of asteroid (101955) Bennu. *Nature* **568**, 55-60 (2019).

12. DellaGiustina, D. N., et al. Properties of rubble-pile asteroid (101955) Bennu from OSIRIS-REx imaging and thermal analysis. *Nature Astronomy* **3**, 341-351 (2019).
13. Reuter, D. C. et al. The OSIRIS-REx Visible and InfraRed Spectrometer (OVIRS): Spectral maps of the asteroid Bennu. *Space Science Reviews* **214**, 55 (2018).
14. Cloutis, E. A. & Gaffey, M. J. Pyroxene spectroscopy revisited: Spectral-compositional correlations and relationship to geothermometry. *Journal of Geophysical Research: Planets* **96**, 22809-22826 (1991).
15. Klima, R. L., Pieters, C. M. & Dyar, M. D. Characterization of the 1.2 µm M1 pyroxene band: Extracting cooling history from near-IR spectra of pyroxenes and pyroxene-dominated rocks. *Meteoritics & Planetary Science* **43**, 1591-1604 (2008).
16. Sunshine, J. M., Pieters, C. M. & Pratt, S. F. Deconvolution of mineral absorption bands: An improved approach. *Journal of Geophysical Research: Solid Earth* **95**, 6955-6966 (1990).
17. Sunshine, J. M. et al. High-calcium pyroxene as an indicator of igneous differentiation in asteroids and meteorites. *Meteoritics & Planetary Science* **39**, 1343-1357 (2004).
18. Burbine, T. H., et al. "Can Formulas Derived From Pyroxenes and/or HEDs Be Used to Determine the Mineralogies of V-Type Asteroids?" *Journal of Geophysical Research: Planets* **123**, 1791-1803 (2018).
19. Brearley, A.J. & Jones, R. H., in Planetary Materials, Vol. 36 (Papike, J.J., ed.), pp. 3.001-3.398 (Mineralogical Society of America, 1998).
20. Cloutis, E. A. et al. Spectral reflectance properties of HED meteorites + CM2 carbonaceous chondrites: Comparison to HED grain size and compositional variations and implications for the nature of low-albedo features on Asteroid 4 Vesta. *Icarus* **223**, 850-877 (2013).
21. Le Corre, L. et al. How to characterize terrains on 4 Vesta using Dawn Framing Camera color bands? *Icarus* **216**, 376-386 (2011).
22. Moskovitz, N. A. et al. A spectroscopic comparison of HED meteorites and V-type asteroids in the inner Main Belt. *Icarus* **208**, 773-788 (2010).
23. Hardersen P. S. et al. Basalt or not? Near-infrared spectra, surface mineralogical estimates, and meteorite analogs for 33 Vp-type asteroids. *The Astronomical Journal* **156**, 11 (2018).
24. Bottke, W. F. et al. In search of the source of asteroid (101955) Bennu: Applications of the stochastic YORP model. *Icarus* **247**, 191-217 (2015).
25. Campins, H. et al. The origin of asteroid 162173 (1999 JU3). *The Astronomical Journal* **146**, 26 (2013).
26. Walsh, K. J., Delbó, M., Bottke, W. F., Vokrouhlický, D. & Lauretta, D. S. Introducing the Eulalia and new Polana asteroid families: Re-assessing primitive asteroid families in the inner Main Belt. *Icarus* **225**, 283-297 (2013).
27. Avdellidou, C., Price, M. C., Delbo, M., Ioannidis, P. & Cole, M. J. Survival of the impactor during hypervelocity collisions–I. An analogue for low porosity targets. *Monthly Notices of the Royal Astronomical Society* **456**, 2957-2965 (2016).
28. Avdellidou, C., Price, M. C., Delbo, M. & Cole, M. J. Survival of the impactor during hypervelocity collisions–II. An analogue for high-porosity targets. *Monthly Notices of the Royal Astronomical Society* **464**, 734-738 (2017).
29. Bottke Jr, W. F., et al. Linking the collisional history of the main asteroid belt to its dynamical excitation and depletion. *Icarus* **179**, 63-94 (2005).
30. Burbine, T. H. et al. in Asteroids III, (W.F. Bottke et al., eds.) pp. 653-668 (Univ. of Arizona Press, 2002).

31. Schenk, P. et al. The geologically recent giant impact basins at Vesta's south pole. *Science* **336**, 694-697 (2012).
32. Spoto, F., Milani, A. and Knežević, Z., Asteroid family ages. Icarus **257**, 257-289 (2015).
33. Bischoff, A., Edward, R. D. S., Metzler, K. & Goodrich, C. A. in Meteorites and the Early Solar System II (Lauretta, D. S. & McSween H. Y. Jr, eds.), pp. 679–712 (Univ. Arizona Press, 2006).
34. Walsh, K. J., et al. Craters, boulders and regolith of (101955) Bennu indicative of an old and dynamic surface. *Nature Geoscience* **12**, 242–246 (2019).
35. Hirata, N., and M. Ishiguro. Properties and possible origin of black boulders on the asteroid Itokawa. Lunar and Planetary Science Conference 42, abstract no. 1821 (2011).
36. De León, J., et al. Expected spectral characteristics of (101955) Bennu and (162173) Ryugu, targets of the OSIRIS-REx and Hayabusa2 missions. *Icarus* **313**, 25-37 (2018).
37. Sugita, S., et al. The geomorphology, color, and thermal properties of Ryugu: Implications for parent-body processes. *Science* **364**, 6437 (2019).
38. Tatsumi, E., et al., Bright boulders suggest a collision between an S-type asteroid and Ryugu's parent body. Nature Astronomy, ***This Issue***
39. Ebert, S., et al. Accretion of differentiated achondritic and aqueously altered chondritic materials in the early solar system—Significance of an igneous fragment in the CM chondrite NWA 12651. *Meteoritics & Planetary Science* **55**, 2985–2995 (2019).
40. Kerraouch, I., et al., A light, chondritic xenolith in the Murchison (CM) chondrite. *Geochemistry* **79**, 125518 (2019).
41. Zolensky, M. E., et al. Mineralogy of carbonaceous chondrite clasts in HED achondrites and the Moon. *Meteoritics & Planetary Science* **31**, 518-537 (1996).

Methods References:

42. Golish, D. R., et al. Ground and In-Flight Calibration of the OSIRIS-REx Camera Suite. *Space Science Reviews* **216**, 12 (2020).
43. Golish, D. R., et al. Disk-resolved photometric modeling and properties of asteroid (101955) Bennu. *Icarus*, In Press doi: https://doi.org/10.1016/j.icarus.2020.113724 (2020).
44. Barnouin, O. S., et al. Shape of (101955) Bennu indicative of a rubble pile with internal stiffness. *Nature Geoscience* **12**, 247-252 (2019).
45. DellaGiustina, D. N., et al. Overcoming the Challenges Associated with Image-Based Mapping of Small Bodies in Preparation for the OSIRIS-REx Mission to (101955) Bennu. *Earth & Space Science* **5**, 929-949 (2018).
46. Daly, M. G., et al. The OSIRIS-REx laser altimeter (OLA) investigation and instrument. *Space Science Reviews* **212**, 899-924 (2017).
47. Christensen, P.R. et al. The OSIRIS-REx thermal emission spectrometer (OTES) instrument. *Space Science Reviews* **214**, 87 (2018).
48. Simon, A.A. et al. OSIRIS-REx visible and near-infrared observations of the Moon. Geophys. Res. Letters 46, 6322-6326 (2019).
49. Sunshine, Jessica M., and Carlé M. Pieters. Estimating modal abundances from the spectra of natural and laboratory pyroxene mixtures using the modified Gaussian model. *Journal of Geophysical Research: Planets* **98**, 9075-9087 (1993).

50. Reddy, V., et al. Mineralogy and surface composition of asteroids, in Asteroids IV (P. Michel et al., eds.), pp. 43-63 (Univ. of Arizona Press, 2015).
51. Pieters, C. M., & T. Hiroi. RELAB (Reflectance Experiment Laboratory): A NASA multiuser spectroscopy facility. Lunar and Planetary Science Conference35, abstract no.1720 (2004).
52. Walsh, K. J., et al. Likelihood for rubble-pile near-earth asteroids to be 1stor Nth generation: focus on Bennu and Ryugu. Lunar and Planetary Science Conference 51, abstract no. 2253 (2020).
53. Bottke, W. F., Nolan, M. C., Greenberg, R., & Kolvoord, R. A. Velocity distributions among colliding asteroids. *Icarus* **107**, 255-268 (1994).
54. Avdellidou, C., Delbo, M. & Fienga, A. Exogenous origin of hydration on asteroid (16) Psyche: the role of hydrated asteroid families. *Monthly Notices of the Royal Astronomical Society* **475**, 3419-3428 (2018).
55. Briani, G., Morbidelli, A., Gounelle, M. & Nesvorny, D. Evidence for an asteroid-comet continuum from simulations of carbonaceous microxenolith dynamical evolution. *Meteoritics & Planetary Science* **46**, 1863-1877 (2011).
56. Gayon-Markt, J., et al. On the origin of the Almahata Sitta meteorite and 2008 TC3 asteroid. *Monthly Notices of the Royal Astronomical Society* **424**, 508-518 (2012).
57. Turrini, D., et al. The contamination of the surface of Vesta by impacts and the delivery of the dark material. *Icarus* **240**, 86-102 (2014).
58. Turrini, D., et al. Olivine on Vesta as exogenous contaminants brought by impacts: Constraints from modeling Vesta's collisional history and from impact simulations. *Icarus* **280**, 328-339 (2016).
59. Nesvorný, D., Miroslav, B., & Valerio C. Identification and dynamical properties of asteroid families. In Asteroids IV (P. Michel et al., eds.) pp. 297-321 (Univ. of Arizona Press, 2015).
60. Daly, R. T., and Schultz, P. H. Delivering a projectile component to the vestan regolith. *Icarus* **264**, 9-19 (2016).
61. Daly, R. T., and Schultz, P. H. The delivery of water by impacts from planetary accretion to present. *Science Advances* **4.4**, eaar2632 (2018).
62. O'Brien, D. P., and Sykes, M. V. The Origin and Evolution of the Asteroid Belt—Implications for Vesta and Ceres. *Space Science Reviews* **163**, 41 (2011).
63. Housen, K. R., Sweet, W. J., Holsapple, K. A. Impacts into porous asteroids. *Icarus* **300**, 72-96 (2018).
64. Avdellidou, C., et al. Very weak carbonaceous asteroid simulants I: Mechanical properties and response to hypervelocity impacts. *Icarus* **341**, 113648 (2020).
65. Bottke, W. F. et al. Interpreting the Cratering Histories of Bennu, Ryugu, and Other Spacecraft-explored Asteroids. The Astronomical Journal, In Press doi: 10.3847/1538-3881/ab88d3
66. Holsapple, K. Theory and equations for craters from impacts and explosions. St. Louis, MO: Washington University (2003).
67. Jutzi, M., Michel, P., Benz, W., Richardson, D.C. Fragment properties at the catastrophic disruption threshold: The effect of the parent body's internal structure. *Icarus* **207**, 54-65 (2010).

Acknowledgements: This material is based upon work supported by NASA under contract NNM10AA11C issued through the New Frontiers Program. The work of C.A. was supported by the French National Research Agency under the project "Investissements d'Avenir" UCA^{JEDI} ANR-15-IDEX-01. C.A. and M.D. would like to acknowledge the French space agency CNES and support from the ANR "ORIGINS" (ANR-18-CE31-0014). M.A.B. also acknowledges support from CNES the French space agency. G. P. acknowledges support from the INAF-Astrophysical Observatory of Arcetri participation, which is supported by Italian Space Agency agreement no. 2017-37-H.0. ET was supported by the JSPS core-to-core program International Planetary Network. The OLA instrument and funding for the Canadian coauthors is provided by the Canadian Space Agency. This research uses spectra acquired at the NASA RELAB facility at Brown University. This work also makes use of data provided by the Minor Planet Physical Properties Catalogue (MP3C) of the Observatoire de la Côte d'Azur. We thank the entire OSIRIS-REx team for making the encounter with Bennu possible.

Author contributions: D.N.D. leads the OSIRIS-REx image processing working group (IPWG) that discovered and characterized exogenic boulders on Bennu using OCAMS data. H.H.K. led the OVIRS spectral analysis that linked the exogenic boulders on Bennu to the HED meteorites. D.R.G, M.P., H.C., L.L.C., N.P., J.L.R.G., E.T., J.d.L., J.L., S.F., B.R., and M.C.N conducted the image processing of OCAMS data. A.A.S. V.E.H., M.A.B., G.P., B.E.C., E.S.H, R.P.B and D.C.R. conducted the spectral characterization and compositional analysis using OVIRS data. W.F.B., C.A., M.D., and K.J.W. conducted the collisional modelling. R.-L.B., R.T.D., E.R.J., T.J.M., and H.C.C. conducted an assessment of the geologic setting. M.G.D, M.M.A.A, L.P., J.S., and O.S.B. produced the OLA digital terrain models. D.S.L. is the Principal Investigator and leads the OSIRIS-REx mission.

Competing interests: The authors declare no competing interests.

Materials and Correspondence: Requests and correspondence should be directed to D. N. DellaGiustina (danidg@lpl.arizona.edu) and H. H. Kaplan (kaplan@boulder.swri.edu).

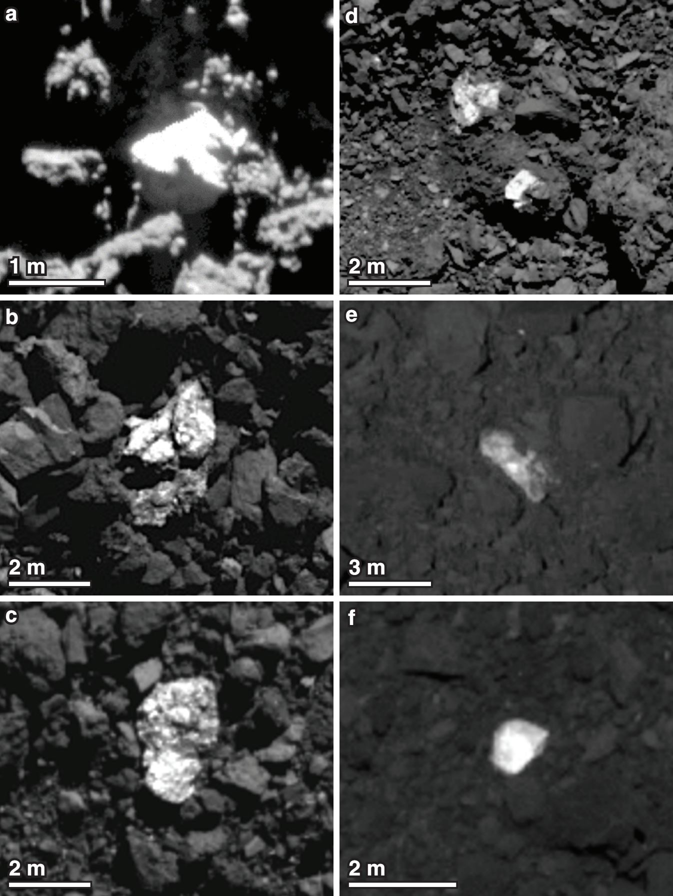
a
1 m
d
2 m
b
2 m
e
3 m
c
2 m
f
2 m

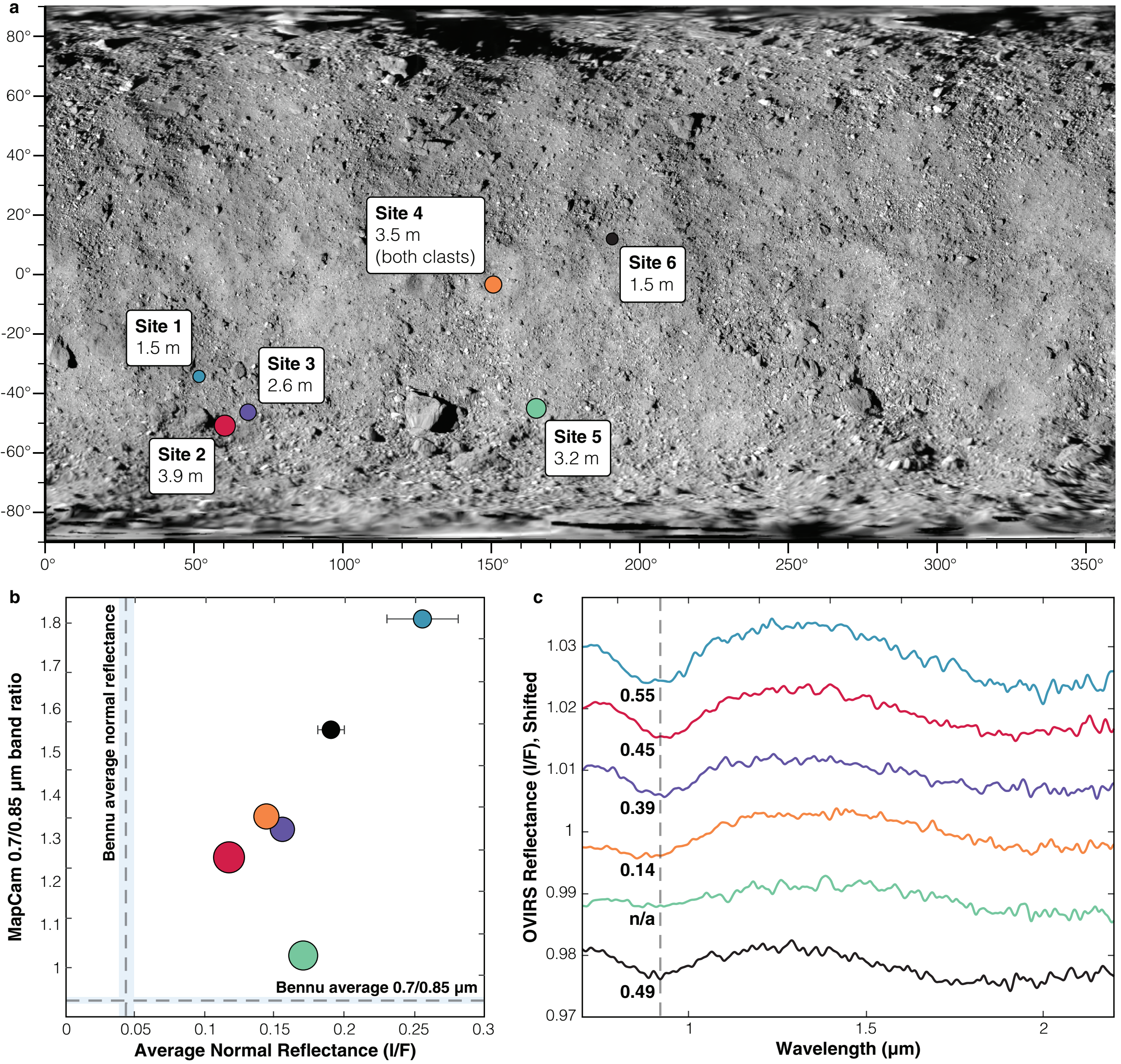
a
80°
60°
40°
20°
0°
-20°
-40°
-60°
-80°
Site 4
3.5 m
(both clasts)
Site 6
1.5 m
Site 1
1.5 m
Site 3
2.6 m
Site 2
3.9 m
Site 5
3.2 m
0°
50°
100°
150°
200°
250°
300°
350°
b
MapCam 0.7/0.85 μm band ratio
Bennu average normal reflectance
Bennu average 0.7/0.85 μm
Average Normal Reflectance (I/F)
1
1.1
1.2
1.3
1.4
1.5
1.6
1.7
1.8
0
0.05
0.1
0.15
0.2
0.25
0.3
c
OVIRS Reflectance (I/F), Shifted
0.55
0.45
0.39
0.14
n/a
0.49
1.03
1.02
1.01
1
0.99
0.98
0.97
1
1.5
2
Wavelength (μm)

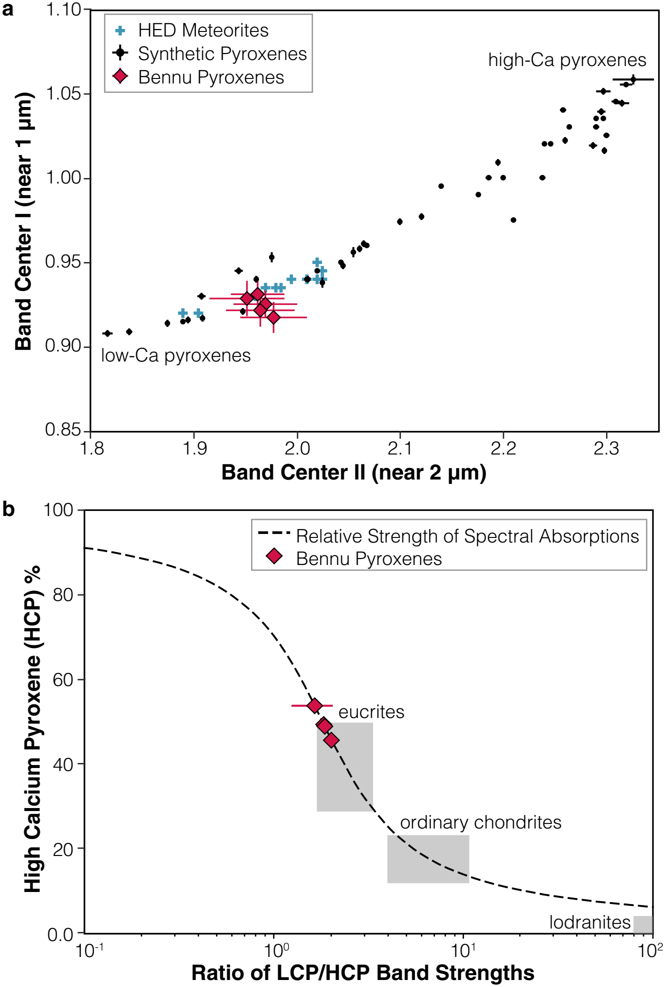
a
HED Meteorites
Synthetic Pyroxenes
Bennu Pyroxenes
high-Ca pyroxenes
low-Ca pyroxenes
Band Center I (near 1 μm)
1.10
1.05
1.00
0.95
0.90
0.85
1.8
1.9
2.0
2.1
2.2
2.3
Band Center II (near 2 μm)
b
Relative Strength of Spectral Absorptions
Bennu Pyroxenes
eucrites
ordinary chondrites
lodranites
High Calcium Pyroxene (HCP) %
100
80
60
40
20
0.0
10^{-1}
10^{0}
10^{1}
10^{2}
Ratio of LCP/HCP Band Strengths

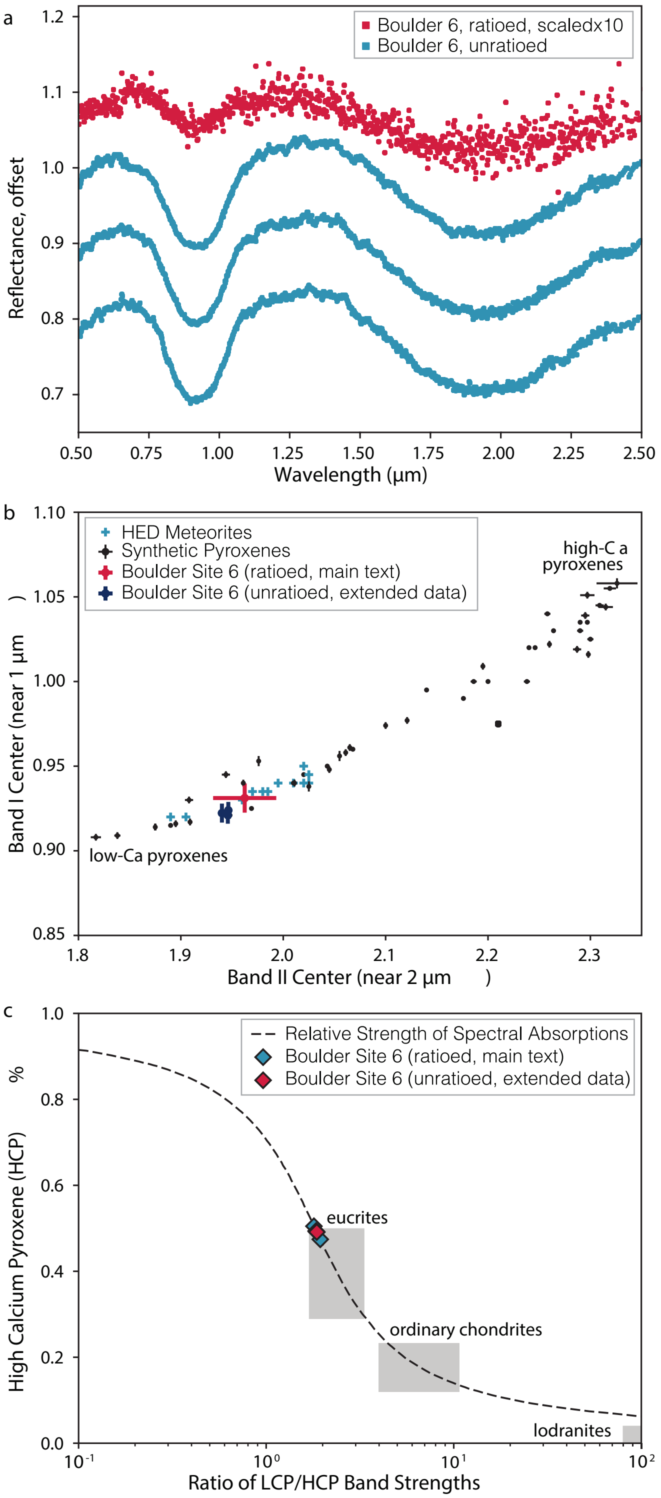
a
Boulder 6, ratioed, scaledx10
Boulder 6, unratioed
Reflectance, offset
0.7
0.8
0.9
1.0
1.1
1.2
0.50
0.75
1.00
1.25
1.50
1.75
2.00
2.25
2.50
Wavelength (μm)
b
HED Meteorites
Synthetic Pyroxenes
Boulder Site 6 (ratioed, main text)
Boulder Site 6 (unratioed, extended data)
high-C a pyroxenes
low-Ca pyroxenes
Band I Center (near 1 μm)
0.85
0.90
0.95
1.00
1.05
1.10
1.8
1.9
2.0
2.1
2.2
2.3
Band II Center (near 2 μm)
c
Relative Strength of Spectral Absorptions
Boulder Site 6 (ratioed, main text)
Boulder Site 6 (unratioed, extended data)
eucrites
ordinary chondrites
lodranites
High Calcium Pyroxene (HCP) %
0.0
0.2
0.4
0.6
0.8
1.0
10⁻¹
10⁰
10¹
10²
Ratio of LCP/HCP Band Strengths